Aerosol measurements with shipborne sun-sky-lunar photometer and collocated multiwavelength Raman polarization lidar over the Atlantic Ocean

Zhenping Yin[1,2,3], Albert Ansmann[1], Holger Baars[1], Martin Radenz[1], Cristofer Jimenez[1], Ronny Engelmann[1], Patric Seifert[1], Alina Herzog[1], Kevin Ohneiser[1], Karsten Hanbuch[1], Luc Blarel[4], Philippe Goloub[4], Gaël Dubois[4], Stephane Victori[5], Fabrice Maupin[5]

[1]Leibniz Institute for Tropospheric Research, Permoserstraße 15, 04318 Leipzig, Germany
[2]School of Electronic Information, Wuhan University, Wuhan, China
[3]Key Laboratory of Geospace Environment and Geodesy, Ministry of Education, Wuhan, China
[4]Laboratoire d'Optique Amosphérique, Université des Sciences et Technologies de Lille, 59655 Villeneuve d'Ascq, France
[5]Cimel advanced monitoring, Paris, France

Correspondence to: Zhenping Yin (zhenping@tropos.de)

Abstract. A shipborne sun-sky-lunar photometer was tested in two trans-Atlantic cruises aboard the German research vessel *Polarstern* from 54°N to 54°S. A full diurnal cycle of mixed dust-smoke episode measured with shipborne CE318-T is presented for the first time. Latitudinal distribution of AOD from the shipborne CE318-T, Raman lidar and MICROTOPS II shows the same trend with high values in the dust belt from 0 ~ 20°N and low values at Southern Hemisphere. Coefficient of determination for the linear regression between MICROTOPS II and shipborne sun-sky-lunar photometer was 0.988, 0.987, 0.994 and 0.994 for AODs at 380, 440, 500 and 870 nm and 0.896 for Ångström exponent at 440-870 nm. Meanwhile, the AOD root-mean-squared differences at 380, 440, 500 and 870 nm are 0.015, 0.013, 0.010 and 0.009.

1 Introduction

Aerosols can influence the Earth radiation budget, e.g., by absorption and scattering of solar radiation, and modulate cloud formation and cloud microphysical properties by serving as cloud condensation nuclei (CCN) or ice nucleating particles (INP). Although great progress has been made in aerosol observation technologies and climate modeling in recent years, the uncertainty of aerosol radiative forcing in global climate models is still very large due to our poor understanding of aerosol global distribution and aerosol-cloud interactions (Stocker, 2014).

Most of the current aerosol observations are land-based. Spaceborne aerosol observations are available but most of them work in low earth orbit, which can not be used to resolve regional aerosol conditions as a function of time. However, the ocean, which covers more than 70 % of our planet earth and works as one of the largest natural aerosol sources, can hardly monitored by land-based instruments. In addition, marine aerosols which are generated from the oceanic white cap and bubble bursting, impose significant contributions to the global direct radiative forcing (Satheesh and Moorthy, 2005). Meanwhile, the transported aerosols from the continent play an important role over the ocean as well, making the aerosol conditions even more complicated. The corresponding measurements for those tiny particles with passive remote sensing intruments can be performed on spaceborne, airborne or shipborne platforms. Spaceborne measurements can provide a global picture of the aerosol conditions over a long-term basis. However, the data retrievals for spaceborne measurements require assumptions about the terrain (Hsu et al., 2013; Sayer et al., 2018), which could bring in non-negligible errors. Airborne measurements have a large coverage (Karol et al., 2013), but the cost for each flight is high and the aircraft is sensitive to the weather conditions, which makes it less available for long-term observations. Shipborne measurements has been performed over a long period of time (Smirnov et al., 2002; Knobelspiesse et al., 2004). Although it's also challenging compared with land-based measurements due to the mobility of the platform and severe weather conditions, huge progress about sun photometer technologies has been made over more than 20 years (Karol et al., 2013; Barreto et al., 2016; Livingston et al., 2003), since the start of the NASA Sensor Inter-comparison and Merger for Biological and Interdisciplinary Oceanic Studies (SIMBIOS) (Fargion et al., 1999), which was dedicated to intercalibration and validation for ocean color satellites. The Maritime Aerosol Network (MAN), as a component of the AErosol RObotic NETwork (AERONET), is the largest long-term aerosol observation network over the ocean (Smirnov et al., 2009). It has provided unique dataset about aerosol optical depth (AOD) and precipitable water vapor (PWV) over the ocean even from Arctic to Antarctica. The data was greatly used in the research about dust transport, satellite retrieval validation and atmospheric correction (Smirnov et al., 2011).

MICROTOPS II is the standard device of MAN. However, it is not dedicated to automatic maritime network observations. At least, an operator needs to point the photometer to the Sun for a while to ensure stable measurements, which makes it less available for continuous measurements. Moreover, it cannot provide aerosol microphysical properties, including size distribution, scattering phase function and single scattering albedo because of missing sky radiance measurements (Smirnov et al., 2009). Therefore, a shipborne photometer based on the advanced sun-sky-lunar photometery technology (CE318-T), was developed to cover this gap by the Laboratoire d'Optique Atmosphérique (LOA), Lille, France. This new device has all the capabilities of a land-based CE318-T (Barreto et al., 2016), like AOD measurement from 340 to 1640 nm, PWV measurement, nighttime AOD measurement and almucantar scanning measurement required for the retrieval of aerosol microphysical properties. Therefore, it's also easy to be incorporated into AERONET. In addtion, this instrument will be moved to the Arctic on-board RV *Polarstern* with joining the unprecedented Arctic research project MOSAiC (https://www.mosaic-expedition.org/). The dataset regarding the Arctic seasonal aerosol conditions will be definitely helpful to quantify our human effects on global climate change. But before that, we need to address how the shipborne CE318-T setup behaves, how much influence of the sea spray could bring and how about the uncertainty of the AOD measurements under oceanic conditions.

In order to answer these questions, this instrument was tested in the framework of the OCEANET project (Macke et al., 2010) during the past two RV *Polarstern* cruises, PS113 and PS116. PS113 started at Punta Arenas, Chile on 7 May 2018 and ended at Bremerhaven, Germany on 11 June 2018. In the case of PS116, RV *Polarstern* departed from Bremerhaven on 11 November 2018 and arrived at Cape Town on 11 December 2018 (see Fig. 1 for the ship tracks). Equipped with sophisticated ground-based instruments, including a portable and automated Raman and polarization lidar system Polly^{XT} (Engelmann et al., 2016; Althausen et al., 2009), microwave radiometer, meteorological station, shadowband radiometer, full-sky imager and MICROTOPS II, it provided a unique opportunity to evaluate the capabilities of the photometer prototype and also provided useful feedback for its future developments.

This paper is organised as follows: In Sect. 2, we give a description of the shipborne CE318-T and other applied instruments and data in this paper. Then in Sect. 3.1, we evaluated the daytime results from the shipborne CE318-T through comparisons with MICROTOPS II and we presented the diurnal measurements of the shipborne CE318-T to validate the nighttime AOD with collocated Raman lidar measurements. In Sect. 3.2, we present two detailed case studies to evaluate the performance of the shipborne CE318-T under pure marine conditions and lofted Saharan dust layers. Besides, we've shown the potential to combine the shipborne CE318-T measurements into lidar data analysis for dust case. Finally, in Sect. 4, summarizing and concluding remarks are given.

2 Instrumentation

The instruments of the OCEANET project are scheduled for investigating aerosol cloud and radiation interactions over the remote Atlantic Ocean and contrasting northern with southern hemispheric aerosol and cloud conditions.The OCEANET project started in the fall of 2009 (Kanitz, 2012). Nearly all the instruments were mounted on the roof of the OCEANET container except the indoor Polly^{XT} lidar. The container was located on the helicopter deck, which is behind the bridge, for these two cruises (see Fig. 2). The MICROTOPS II measurements were conducted on the bridge (see Fig. 2). It should be noted that the 'anthropogenic' smoke from the funnel could contaminate the shipborne CE318-T measurements. However, this was a compromise between avoiding strong head winds, sea spray and smoke. Nevertheless, we only found an AOD shift of 0.002 at 500 nm between shipborne CE318-T and MICROTOPS II, which shows the influence of the smoke was negligible.

2.1 Shipborne CE318-T

The shipborne CE318-T is developed to enable AOD measurement over the mobile platform and expand the AERONET coverage to the vast ocean area (Goloub et al., 2017). In principle, the instrument is very similar to the traditional CE318-T (Barreto et al., 2016) and has nearly the same steps for installation. The apparatus consists of the optical head, rotational base, control unit, air pumping component, weather stop component, compass and GPS modules (see Fig. 3). The optical head was the same like the other land-based CE318-T. The GPS receiver and compass module (SIMRAD HS60) were fixed on the platform together with the photometer robot to assure the same motions. In order to track the sun continuously over the ship, the photometer will firstly go to the sun with the last information (date, time, geolocation, heading, pitch and roll) from the GPS receiver and compass module. This can help the photometer point to the sun if the ship does not turn quickly. If the photometer does not see the sun, which can be determined through the digital number from direct sun measurements, the head will be controlled to search the sky at 45º in the left and right horizontal panels. When it detects the sun, the new position will be used to calculate the turning angle of the ship and then to correct the azimuth position for next measurements. When the sun is in the tracking field of view (~ 10º), the photometer will switch into tracking mode like a regular photometer. However, what's unlike a conventional CE318-T is, the tracking mode by using the 4-quadrant detector, will keep working to compensate the motions of the ship during all the SUN triplet measurements. It is the same procedure for MOON triplet as well. The air pumping module generates compressed dry-clean air to the collimator to prohibit the contamination of optical window by ambient sea spray. Meanwhile, we changed the wet sensor (a resistor) by an optical rain sensor to prevent the influence of the strong corrosion from the sea spray. Besides, we added an anemometer to help stop the system, because the robot itself will vibrate as wind speed increases above 45 km/h. But over the two measurement cruises, we chose the limit of 40 km/h to keep it safe.

The photometer arrangement is very robust and robotic to conduct 24/7 measurement without special care. The new rain sensor and anemometer worked quite well as being tested under oceanic stormy and rainy weather conditions. The collected data was finally transferred to the LOA server for further analysis.

This prototype has 10 channels with nominal wavelengths of 340, 380, 440, 500, 532, 670, 870, 937, 1020, 1064 nm. It can provide AOD values at nine wavelengths and PWV at both daytime and nighttime. It also has the potential of performing almucantar scanning. Further efforts and investigations would be necessary to utilise these data for aerosol microphysical research. The data processing followed the same procedure described in Barreto et al. (2016). In addition, we need to save the geolocation data along with the AOD since the platform keeps moving all the time.

2.2 MICROTOPS II

AOD and PWV measurements were also performed with a handheld MICROTOPS II (Ichoku et al., 2002; Smirnov et al., 2002) from the framework of MAN, which was proceeded by SIMBIO (Sensor Intercalibration and Merger for Biological and Interdisciplinary Oceanic Studies) (Fargion et al., 2001; Knobelspiesse et al., 2004). It was calibrated before and after the cruise by NASA Goddard Space Flight Center. This type of MICROTOPS II has 5 channels at 380, 440, 675, 870 and 936 nm.

There are three data quality levels for the AOD both from shipborne CE318-T and MICROTOPS II: Level 1.0 with no cloud screening, Level 1.5 with cloud screening and Level 2.0 (Level 1.6 for shipborne CE318-T) for cloud screening and quality assurance (Smirnov et al., 2011). We used Level 2.0 (Level 1.6 for shipborne CE318-T) AOD at 380, 440, 500 and 870 nm for our analysis below and we need to point out that 500 nm AOD from MICROTOPS II database was interpolated with using the Ångström exponent.

2.3 Polly^{XT}

The Raman polarization lidar (Polly^{XT}) was continuously operated during the entire cruise. The Polly^{XT} has two telescopes with diameter of 50 and 300 mm, respectively. There are 12 detection channels connected with these two telescopes, to cover the detection range from near surface to 4 km (near-range) and from 800 m to more than 10 km (far-range). It has 8 far-range channels with wavelengths at 355 nm (total: elastic signal and cross: filtered by a polarizer), 387 nm, 407 nm, 532 nm (total and cross), 607 nm and 1064 nm, 4 near-range channels with wavelengths at 355 nm, 387 nm, 532 nm and 607 nm (Engelmann et al., 2016). The signal can be used to retrieve the vertical profiles of volume depolarization ratios at 355- and 532 nm, extinction coefficients at 355- and 532 nm, backscatter coefficients at 355-, 532- and 1064 nm, which are related with aerosol bulk properties. Hence, particle depolarization ratios at 355- and 532nm and lidar ratios at 355- and 532 nm can be retrieved, which are sensitive to particle size, shape and chemistry properties (Freudenthaler et al., 2009; Baars et al., 2016). The backscatter coefficient β and extinction coefficient α are good indicators for particle concentration (Ansmann and Müller, 2005). The lidar ratio S, which is the ratio of extinction and backscatter coefficient, describes the particle absorption ability (Müller et al., 2007; Groß et al., 2011a). Absorbing particles like soot and black-carbon-containing particles have a higher lidar ratio than non-absorbing sulfate aerosol particles. Ångström exponent Å (Angstrom, 1964) which describes the relationship between optical properties (backscatter, extinction) at two wavelengths can be used as an indicator for particle size (Baars et al., 2016; Ansmann et al., 2002). Normally, large particles like dust particles, have a small Å (< 0.5). On the contrary, small particles like biomass combustion aerosols, most continental aerosols, have a larger Å (> 1.0) (Müller et al., 2007; Baars et al., 2016; Eck et al., 1999). Therefore, aerosol layers with different physical and chemical properties, like marine aerosol, dust and smoke, can be characterized based on these retrieving results.

The near-range telescope can suppress the incomplete overlap zone to 120 m, which enabled us to capture the aerosol distribution and evolution inside the marine boundary layer (MBL) (Kanitz et al., 2013; Engelmann et al., 2016). In order to avoid the damage for the photon-counting detectors from strong solar radiation, the lidar system was turned off when the solar elevation angle exceeded 70° and the 407 nm channel was turned off routinely at daytime.

In order to calculate the AOD, Raman method (Ansmann et al., 1992) and Fernald method (Fernald et al., 1972) were utilized for nighttime and daytime measurements, respectively. Fernald method needs the assumption of lidar ratio, which is dependent on aerosol types. In our analysis, lidar ratios of 20 sr (20 and 20 sr), 50 sr (50 and 50 sr) were used for marine aerosols and dust at 355 nm (532 and 1064 nm) (Groß et al., 2011a). This would lead to an relative error of 20% for AOD, which is dependent on the deviations of lidar ratio for the aerosol layers (Kafle and Coulter, 2013; Hughes et al., 1985). Raman method can achieve better accuracy, because it doesn't need the critical assumption (Ansmann et al., 1992). However, it can lead to relatively large statistical error, due to the very weak Raman signal. Therefore, in order to make the statistical error less than 15%, we accumulated the signal within 1 hour and used vertical smoothing window to increase the signal-noise-ratio (Mattis et al., 2004; Groß et al., 2011b).

2.4 Supplementary instruments and data sources

Temperature, pressure and relative humidity (RH) profiles were obtained from radiosonde ascents. The radiosondes were launched on board the RV *Polarstern* at 11:00 UTC on each day. In order to have better temporal resolved meteorological information, Global Data Assimilation System 1° resolution (GDAS1) meteorology data (Kanamitsu, 1989) was used in the lidar data analysis. This data is processed every three hours per day with a spatial resolution of 1° (latitude, longitude) by an atmospheric model provided by National Centers for Environmental Prediction (NCEP). In addition, the Hybrid Single-Particle Lagrangian Integrated Trajectory (HYSPLIT) model (Draxler, 2011) was used for backward trajectory analysis.

3 Results

3.1 Validation of shipborne CE318-T

3.1.1 Daytime validation with MICROTOPS II

The AOD measurements were conducted with MICROTOPS II, Polly^{XT} and shipborne CE318-T simultaneously at daytime and with Polly^{XT} and shipborne CE318-T at nighttime. In order to evaluate the reliability and data quality of the shipborne CE318-T, we showed linear regressions between MICROTOPS II AOD and shipborne CE318-T AOD in Fig. 4. Good linear relationship was found between the shipborne CE318-T and MICROTOPS II with R^2 (coefficient of determination) of 0.988, 0.987, 0.994 and 0.994 for AODs at 380, 440, 500 and 870 nm and of 0.896 for the Ångström exponent. The Ångström exponent is sensitive to the measurement error at clean conditions with AOD less than 0.05. Therefore the scatter in the respective correlation in Fig. 4e is acceptable.

In order to study how the AOD from these two instruments agreed with each other, we used the Bland-Altman plots (Willmott, 1982; Knobelspiesse et al., 2019; Bland and Altman, 1986) to visualize AOD difference ($\Delta\mathrm{AOD} = \mathrm{AOD}_{\mathrm{CE318-T}} - \mathrm{AOD}_{\mathrm{MICROTOPS}}$) against the AOD mean ($\overline{\mathrm{AOD}} = (\mathrm{AOD}_{\mathrm{CE318-T}} + \mathrm{AOD}_{\mathrm{MICROTOPS}})/2$, which can clearly display the bias and system effects. We only took the data pairs with the 500 nm AOD between 0.04 and 0.2, according to the WMO criteria for traceability (WMO). Besides, we used the metric, which is the percentage of $\overline{\mathrm{AOD}}$ that falls out of the boundary of the mean difference $\pm$ 1.96 $\times$ the root-mean-squared AOD difference, to indicate the agreement of two measurements. If the measurement differences are normally distributed, we can use the criteria of 5% to indicate whether the agreement is good or not (Giavarina, 2015). However, our measurements failed the normality test, which stated potential systematic errors either from MICROTOPS II or from the shipborne CE318-T, but we still keep using this metric to indicate the agreement.

From Fig. 5, we found small positive bias of 0.0019, 0.0050, 0.0052 and 0.0027 for AODs at 380, 440, 500 and 870 nm compared with MICROTOPS II and the root-mean-squared AOD differences are 0.0149, 0.0128, 0.0099 and 0.0090, respectively. Based on the research from Morys et al. (2001) and Ichoku et al. (2002), the estimated uncertainties of AOD from MICROTOPS II were about 0.02 at 340 nm and decreasing to about 0.01 at 870 nm while comparing with the AERONET field instrument, which means we can only validate other instrument to this level with taking the MICROTOPS II as the reference. Besides, the falling out percentages of the AOD difference were 3.80%, 3.80%, 7.59% and 2.53%. These results stated the AODs at 380, 440 and 870 nm from the shipborne CE318-T were in good agreement with MICROTOPS II. AOD at 500 nm was a little bit worse, as the falling out percentage exceeded 5%. But as we mentioned in Sect. 2.2, the 500 nm AOD from the MICROTOPS II was interpolated from other wavelengths, we don’t know how much influence it would bring. Overall, we can conclude the daytime capabilities for the shipborne CE318-T under the real marine conditions are as good as the MICROTOPS II.

3.1.2 Nighttime comparisons with Polly^{XT}

This shipborne CE318-T has the capability to conduct nighttime measurement as well. This feature can help us to investigate the diurnal evolution of marine aerosols and dust layers over the ocean. However, this function is more challenging than the daytime measurement as moon tracking is much more sensitive to errors of the leveling adjustment, coordination and orientation data from the compass. Therefore, we need to analyze the accuracy of the nighttime measurements. In Fig. 6, we presented the full diurnal measurements from the shipborne CE318-T, Polly^{XT} and MICROTOPS II at 26 November 2018. On this day, RV *Polarstern* had just passed Cape Verde and was heading towards Cape Town. A mixed layer of dust and pollution aerosol was observed over the whole day. This finding is corroborated by the 532 nm volume linear depolarization ratio plot in Fig. 6c and backward trajectories in Fig. 7. The backward trajectories shows that the air mass between 1 and 3 km on 26 November 2018 originated from the Saharan desert and were over Chad and Niger six days before crossing RV *Polarstern*. All the backward trajectories including the ones for 500 m and 1000 m arrival height crossed the active biomass burning regions two days before arriving RV *Polarstern*. Therefore, the advected dust layer probably took up a large amount of biomass-burning aerosols over central Africa. In order to evaluate the shipborne CE318-T AOD measurements at nighttime, AOD from Polly^{XT} was calculated based on the extinction coefficient retrieved with Raman method (Ansmann et al., 1992). Above 1.5 km to 6 km, the extinction coefficient was taken from far-range channel result and between 0.3 and 1.5 km, the near-range retrieving results was used. Below 0.3 km, the extinction coefficient was considered to be constant, as displayed in Fig. 8b. Besides, we've checked the signal above 6 km and found no additional aerosol layers. The overall relative error of AOD with using this approach was 11-15%, according to the error analysis from (Ansmann et al., 1992; Mattis et al., 2004; Groß et al., 2011b). The time series of AOD can be found in Fig. 6a. The deviation between nighttime shipborne CE318-T and lidar observations was less than 0.03. Daytime measurements from the shipborne CE318-T are also in good agreement with MICROTOPS II at 11:00 UTC with a deviation of 0.01 and 0.01 for the 500 nm AOD and the Ångström exponent respectively.

3.2 Case studies

In Fig. 9, the latitudinal distribution of AOD at 500 nm (532 nm) from these three instruments is displayed for the data collected during the two RV *Polarstern* cruises, PS113 and PS116. In both Fig. 9a and Fig. 9b, all measurements show the same trend with peak values between 0° and 20°N (Kanitz et al., 2013), which is the outflow region of Saharan dust and large amount of biomass-burning aerosols. For PS113, this belt was mainly filled with dust particles, because the Ångström exponent at 440-870 nm was less than 0.4 and AOD was over 0.5, which was typical for Saharan dust (Toledano et al., 2007; Rittmeister et al., 2017). However, for PS116, the air mass in this belt showed a mixture of dust and smoke because the Ångström exponent at 440-870 nm was larger than 1 (Baars et al., 2012). This finding is corroborated by the lidar measurements and backward trajectories as well. On the contrary, the southern hemisphere contains less anthropogenic aerosols and dust. Under most cases, marine aerosol dominates. Nevertheless, lofted biomass burning aerosols from Brazil at 25°S during PS113 was also captured by Polly^{XT} with a layer top height of 2 km, which is not shown here.

In order to illustrate the aerosol vertical distribution over the Atlantic Ocean and investigate the behavior of shipborne CE318-T at different aerosol conditions, we present the results from shipborne CE318-T, lidar and MICROTOPS II observations at pure marine condition and in cases with Saharan dust outbreaks. Detailed analysis was applied based on the diurnal measurements from the shipborne CE318-T and Polly^{XT} lidar and daytime measurements from MICROTOPS II.

3.2.1 Marine aerosol conditions

On 23 November 2018, RV *Polarstern* was west of Western Sahara and approaching Cape Verde. Northwestern airflow and clean marine conditions prevailed. The measurements from shipborne CE318-T and lidar were shown in Fig. 10. According to the 532 nm attenuated backscatter, typical marine aerosol conditions were observed. The 532 nm volume depolarization ratio was less than 0.05 below 1.8 km, which means that the marine boundary layer was dominated by spherical sea salt particles. The backward trajectories in Fig. 11 show that the air mass was mainly carried over the ocean during the past 4 days. Furthermore, no strong aerosol layers were observed above 2 km height. The mean AOD at 532 nm from 08:30 to 11:00 UTC based on shipborne CE318-T measurements was 0.06 ± 0.01 and mean Ångström exponent at 440-870 nm was 0.26 ± 0.03, These are typical values for marine aerosols, which are dominated by coarse mode sea salt particles (Smirnov et al, 2006). The mean AOD at 532 nm and mean Ångström exponent at 440-870 nm from MICROTOPS II were 0.05 ± 0.01 and 0.20 ± 0.03, which are in good agreement with the shipborne CE318-T.

Detailed height-resolved aerosol information was displayed in Fig. 12. According to the RH profile in Fig. 12d, the marine layer reached to about 2 km height. The mean extinction coefficient was 38.5 Mm^{-1}, 27.4 Mm^{-1} and 19.2 Mm^{-1} at 355 nm, 532 nm and 1064 nm, by using Fernald method (Fernald et al., 1972) and assuming a fixed lidar ratio of 20 sr (Groß et al., 2011a). The particle depolarization ratios below 1.6 km were less than 0.02 at 355 nm and 532 nm. From 1.7 km to 2.0 km, the particle depolarization ratio increased with peak value at 355 nm (532 nm) to be 0.09 (0.08) and RH decreased to 10 % according to the GDAS1 data. These are good indicators for dried sea salt particles (Haarig et al., 2017; Bohlmann et al., 2018). When RH drops below 45 %, the spherical marine aerosol particles start to crystallize and become cubic-like in shape. These cubic dry sea salt particles will introduce a relatively strong depolarized signal and lead to the increase of particle depolarization ratio (Haarig et al., 2017).

3.2.2 Saharan dust

When the RV *Polarstern* approached Cape Verde Islands, a dust outbreak was observed from 27 May to 31 May 2018. The whole event started with a mixture of dust and smoke above the MBL. Since 30 May 2018, the layer was lofted to 1.5 km and started to be dominated by pure Saharan dust particles.

The MICROTOPS II, shipborne CE318-T and lidar measurements from 16:00 to 17:00 UTC on 30 May 2018 are displayed in Fig. 13. According to Fig. 13a, the results from the shipborne CE318-T and MICROTOPS II agreed well with mean AOD of 0.66 ± 0.03 and 0.62 ± 0.02 and mean Ångström exponent at 440-870 of 0.08 ± 0.02 and 0.07 ± 0.01. Both results indicate the presence of a large amount of large dust particles. In Fig 13c, we can see a layer, located between 0.6 km to 1 km causing slightly enhanced volume depolarization ratio and a dust layer located between 1.5 and 5 km with large volume depolarization ratio. Inside the MBL, the volume depolarization ratio was quite low which indicates that the contamination caused by dust sedimentation was small.

In Fig. 14, we present the averaged vertical profiles from lidar. The extinction coefficient was retrieved by Fernald method with assuming the lidar ratios of 60 sr (355 nm), 45 sr (532 nm) and 54 sr (1064 nm) for the dust layer and 25 sr (355, 532, 1064 nm) for the MBL. The lidar ratios at 355 and 532 nm were selected based on nighttime Raman retrieving results, and the lidar ratio at 1064 nm was from AERONET measurements (Shin et al., 2018). Meanwhile, reference values were tuned to achieve the best agreement of AOD between lidar and shipborne CE318-T. Inside the MBL, the mean extinction coefficients at 355 nm and 532 nm are 245 Mm^{-1} and 241 Mm^{-1} according to Fig. 14a, which is very large compared to pure marine conditions in Sect. 3.2.1. This might be caused by the loading and hygroscopic growth of anthropogenic aerosols. This assumption is corroborated by the backward trajectories in Fig. 15a, because a branch of the backward trajectories arriving at 500 m can be traced back to European continent. The lofted dust layer extended from 1.5 to 5 km with mean extinction coefficients at 355 nm, 532 nm and 1064 nm to be 166 Mm^{-1}, 161 Mm^{-1} and 159 Mm^{-1} and particle depolarization ratios at 355 nm and 532 nm to be 0.21 ± 0.05 and 0.31 ± 0.05, which are in good agreement with optical properties for pure Saharan dust (Groß et al., 2011a; Groß et al., 2011b; Tesche et al., 2009). The backward trajectories in Fig. 15b showed the air mass at 4 km originated from Chad, Libya and Sudan, and travelled 5 days from these regions before reaching RV *Polarstern*. A relatively clean layer can be found between the lofted dust layer and MBL with extinction coefficient and particle depolarization ratio less than 25 Mm^{-1} and 0.04, respectively. Therefore, we are convinced that the sedimentation of dust particles was negligible. Above the MBL, from 0.5 km to 1 km, there was an aerosol layer with enhanced particle depolarization ratio at 355 nm (532 nm) of 0.11 (0.15). The backward trajectories for this layer was similar with Fig. 15a. Therefore, it probably consisted of relatively dry aged anthropogenic particles or mixture of dry aged anthropogenic particles and dry sea salt particles.

4 Conclusions

Shipborne CE318-T measurements were conducted during two trans-Atlantic RV *Polarstern* cruises together with collocated $Polly^{XT}$ lidar and independent MICROTOPS II. The shipborne CE318-T has a special design to avoid contamination of sea-spray and achieved the goal of automatic measurement over the ocean during the entire 4-5 weeks periods of the two cruises. From linear regression and Bland-Altman plot, we found the capabilities of the shipborne CE318-T under the real oceanic conditions were as good as the manually operated MICROTOPS II to capture the daytime AOD variabilities. For nighttime measurements, deviations between the 532 nm AOD observed with $Polly^{XT}$ and the shipborne CE318-T was found to be less than 10 %.

The almucantar scanning option will also be implemented in near future, which allow the retrieval of aerosol microphysical properties over the ocean. All of these features will significantly increase our potential to characterize marine aerosol distribution over the remote ocean and the impact of continental dust, smoke, and haze outbreaks on the aerosol conditions far away from the continent, as well as dust transport and dust sedimentation over the less exploited oceans.

Data availability. Radiosonde and lidar data for the two cruises are available at the Leibniz Institute for Tropospheric Research and can be accessed upon request. MICROTOPS II data can be downloaded from the AERONET MAN database (MAN). The shipborne CE318-T data can be accessed through contact with Philippe (philippe.goloub@univ-lille.fr).

Author contributions. ZP performed the lidar data analysis and prepared the manuscript with great support from AA. MR, CJ and ZP set up the instruments for PS113 and were responsible for the lidar measurements. AH, KO and KH set up the instruments during PS116 and were responsible for the lidar measurements during PS116. PG, LB, GD, SV and FM built up the shipborne CE318-T and were responsible for the corresponding data analysis. All authors contributed to scientific discussion and in this way to the manuscript preparation.

Competing interests. The authors declare that they have no conflict of interests.

Acknowledgements. The authors acknowledge funding from ACTRIS under grant agreement no. 262254, ACTRIS-2 under grant agreement no. 654109 from the European Union's Horizon 2020 research and innovation programme, Labex CaPPA (The CaPPA project (Chemical and Physical Properties of the Atmosphere) and ESA/IDEAS program. We sincerely thank the Alfred Wegener Institute and the RV *Polarstern* crewmembers for their huge support and effort in PS113 and PS116 (acknowledgement no. AWI_PS113_00, AWI_PS116_00). We also appreciate the effort of the AERONET MAN, HYSPLIT teams to provide the additional research data to solid the analysis in the paper. Besides, Zhenping Yin appreciates the support from the Chinese Scholarship Council (CSC) to conduct this research under the CSC no. 201706270117.

References

Althausen, D., Engelmann, R., Baars, H., Heese, B., Ansmann, A., Müller, D., and Komppula, M.: Portable Raman lidar PollyXT for automated profiling of aerosol backscatter, extinction, and depolarization, Journal of Atmospheric and Oceanic Technology, 26, 2366-2378, https://doi.org/10.1175/2009jtecha1304.1, 2009.

Angstrom, A.: The Parameters of Atmospheric Turbidity, Tellus, 16, 64-75, https://doi.org/10.1111/j.2153-3490.1964.tb00144.x, 1964.

Ansmann, A., Riebesell, M., Wandinger, U., Weitkamp, C., Voss, E., Lahmann, W., and Michaelis, W.: Combined Raman Elastic-Backscatter Lidar for Vertical Profiling of Moisture, Aerosol Extinction, Backscatter, and Lidar Ratio, Appl Phys B-Photo, 55, 18-28, https://doi.org/10.1007/Bf00348608, 1992.

Ansmann, A., Wagner, F., Müller, D., Althausen, D., Herber, A., von Hoyningen-Huene, W., and Wandinger, U.: European pollution outbreaks during ACE 2: Optical particle properties inferred from multiwavelength lidar and star-Sun photometry, Journal of Geophysical Research: Atmospheres, 107, AAC 8-1-AAC 8-14, https://doi.org/10.1029/2001jd001109, 2002.

Ansmann, A., and Müller, D.: Lidar and atmospheric aerosol particles, in: Lidar, Springer, 105-141, 2005.

Baars, H., Ansmann, A., Althausen, D., Engelmann, R., Heese, B., Muller, D., Artaxo, P., Paixao, M., Pauliquevis, T., and Souza, R.: Aerosol profiling with lidar in the Amazon Basin during the wet and dry season, J Geophys Res-Atmos, 117, https://doi.org/10.1029/2012jd018338, 2012.

Baars, H., Kanitz, T., Engelmann, R., Althausen, D., Heese, B., Komppula, M., Preissler, J., Tesche, M., Ansmann, A., Wandinger, U., Lim, J. H., Ahn, J. Y., Stachlewska, I. S., Amiridis, V., Marinou, E., Seifert, P., Hofer, J., Skupin, A., Schneider, F., Bohlmann, S., Foth, A., Bley, S., Pfuller, A., Giannakaki, E., Lihavainen, H., Viisanen, Y., Hooda, R. K., Pereira, S. N., Bortoli, D., Wagner, F., Mattis, I., Janicka, L., Markowicz, K. M., Achtert, P., Artaxo, P., Pauliquevis, T., Souza, R. A. F., Sharma, V. P., van Zyl, P. G., Beukes, J. P., Sun, J. Y., Rohwer, E. G., Deng, R. R., Mamouri, R. E., and Zamorano, F.: An overview of the first decade of Polly(NET): an emerging network of automated Raman-polarization lidars for continuous aerosol profiling, Atmospheric Chemistry and Physics, 16, 5111-5137, https://doi.org/10.5194/acp-16-5111-2016, 2016.

Barreto, A., Cuevas, E., Granados-Munoz, M. J., Alados-Arboledas, L., Romero, P. M., Grobner, J., Kouremeti, N., Almansa, A. F., Stone, T., Toledano, C., Roman, R., Sorokin, M., Holben, B., Canini, M., and Yela, M.: The new sun-sky-lunar Cimel CE318-T multiband photometer - a comprehensive performance evaluation, Atmospheric Measurement Techniques, 9, 631-654, https://doi.org/10.5194/amt-9-631-2016, 2016.

Bland, J. M., and Altman, D.: Statistical methods for assessing agreement between two methods of clinical measurement, The lancet, 327, 307-310, https://doi.org/10.1016/s0140-6736(86)90837-8, 1986.

Bohlmann, S., Baars, H., Radenz, M., Engelmann, R., and Macke, A.: Ship-borne aerosol profiling with lidar over the Atlantic Ocean: from pure marine conditions to complex dust-smoke mixtures, Atmospheric Chemistry and Physics, 18, 9661-9679, https://doi.org/10.5194/acp-18-9661-2018, 2018.

Draxler, R. R.: Hysplit (hybrid single-particle lagrangian integrated trajectory) model access via NOAA ARL ready website, https://ready.arl.noaa.gov/HYSPLIT.php, 2011.

Eck, T. F., Holben, B. N., Reid, J. S., Dubovik, O., Smirnov, A., O'Neill, N. T., Slutsker, I., and Kinne, S.: Wavelength dependence of the optical depth of biomass burning, urban, and desert dust aerosols, J Geophys Res-Atmos, 104, 31333-31349, https://doi.org/10.1029/1999jd900923, 1999.

Engelmann, R., Kanitz, T., Baars, H., Heese, B., Althausen, D., Skupin, A., Wandinger, U., Komppula, M., Stachlewska, I. S., Amiridis, V., Marinou, E., Mattis, I., Linne, H., and Ansmann, A.: The automated multiwavelength Raman polarization and water-vapor lidar Polly(XT): the neXT generation, Atmospheric Measurement Techniques, 9, 1767-1784, https://doi.org/10.5194/amt-9-1767-2016, 2016.

Fargion, G. S., McClain, C. R., Fukushima, H., Nicolas, J. M., and Barnes, R. A.: Ocean color instrument intercomparisons and cross-calibrations by the SIMBIOS Project, Sensors, Systems, and Next-Generation Satellites III, 1999, 397-403, Fargion, G. S., Barnes, R., and McClain, C.: In Situ Aerosol Optical Thickness Collected by the SIMBIOS Program (1997-2000): Protocols, and and Data QC and Analysis, 2001.

Fernald, F. G., Herman, B. M., and Reagan, J. A.: Determination of aerosol height distributions by lidar, Journal of Applied meteorology, 11, 482-489, https://doi.org/10.1175/1520-0450(1972)011%3C0482:doahdb%3E2.0.co;2, 1972.

Freudenthaler, V., Esselborn, M., Wiegner, M., Heese, B., Tesche, M., Ansmann, A., Muller, D., Althausen, D., Wirth, M., Fix, A., Ehret, G., Knippertz, P., Toledano, C., Gasteiger, J., Garhammer, M., and Seefeldner, M.: Depolarization ratio profiling at several wavelengths in pure Saharan dust during SAMUM 2006, Tellus Series B-Chemical and Physical Meteorology, 61, 165-179, https://doi.org/10.1111/j.1600-0889.2008.00396.x, 2009.

Giavarina, D.: Understanding bland altman analysis, Biochemia medica: Biochemia medica, 25, 141-151, https://doi.org/10.11613/bm.2015.015, 2015.

Goloub, P., Blarel, L., Dubios, G., Popovici, I., Podvin, T., Torres, B., Victori, S., Maupin, F., and Pikridas, M.: Current results on mobile system prototype development for Aerosol Cal/Val activities, ESA/IDEAS Project WP 3440-1/3/5, 12 Dec, 2017, 2017.

Groß, S., Tesche, M., Freudenthaler, V., Toledano, C., Wiegner, M., Ansmann, A., Althausen, D., and Seefeldner, M.: Characterization of Saharan dust, marine aerosols and mixtures of biomass-burning aerosols and dust by means of multi-wavelength depolarization and Raman lidar measurements during SAMUM 2, Tellus B: Chemical and Physical Meteorology, 63, 706-724, https://doi.org/10.3402/tellusb.v63i4.16369, 2011a.

Groß, S., Wiegner, M., Freudenthaler, V., and Toledano, C.: Lidar ratio of Saharan dust over Cape Verde Islands: Assessment and error calculation, Journal of Geophysical Research: Atmospheres, 116, https://doi.org/10.1029/2010JD015435, 2011b.

Haarig, M., Ansmann, A., Gasteiger, J., Kandler, K., Althausen, D., Baars, H., Radenz, M., and Farrell, D. A.: Dry versus wet marine particle optical properties: RH dependence of depolarization ratio, backscatter, and extinction from multiwavelength lidar measurements during SALTRACE, Atmospheric Chemistry and Physics, 17, 14199, https://doi.org/10.5194/acp-2017-545, 2017.

Hughes, H. G., Ferguson, J. A., and Stephens, D. H.: Sensitivity of a lidar inversion algorithm to parameters relating atmospheric backscatter and extinction, Applied optics, 24, 1609-1613, https://doi.org/10.1364/ao.24.001609, 1985.

Ichoku, C., Levy, R., Kaufman, Y. J., Remer, L. A., Li, R. R., Martins, V. J., Holben, B. N., Abuhassan, N., Slutsker, I., and Eck, T. F.: Analysis of the performance characteristics of the five-channel Microtops II Sun photometer for measuring aerosol optical thickness and precipitable water vapor, Journal of Geophysical Research: Atmospheres, 107, AAC 5-1-AAC 5-17, https://doi.org/10.1029/2001jd001302, 2002.

Kafle, D., and Coulter, R.: Micropulse lidar-derived aerosol optical depth climatology at ARM sites worldwide, Journal of Geophysical Research: Atmospheres, 118, 7293-7308, https://doi.org/10.1002/jgrd.50536, 2013.

Kanamitsu, M.: Description of the NMC global data assimilation and forecast system, Weather and Forecasting, 4, 335-342, https://doi.org/10.1175/1520-0434(1989)004%3C0335:dotngd%3E2.0.co;2, 1989.

Kanitz, T.: Vertical distribution of aerosols above the Atlantic Ocean, Punta Arenas (Chile), and Stellenbosch (South Africa). Characterization, solar radiative effects and ice nucleating properties, https://doi.org/10.14279/depositonce-3386, 2012.

Kanitz, T., Ansmann, A., Engelmann, R., and Althausen, D.: North-south cross sections of the vertical aerosol distribution over the Atlantic Ocean from multiwavelength Raman/polarization lidar during Polarstern cruises, J Geophys Res Atmos, 118, 2643-2655, https://doi.org/10.1002/jgrd.50273, 2013.

Karol, Y., Tanré, D., Goloub, P., Vervaerde, C., Balois, J., Blarel, L., Podvin, T., Mortier, A., and Chaikovsky, A.: Airborne sun photometer PLASMA: concept, measurements, comparison of aerosol extinction vertical profile with lidar, Atmospheric Measurement Techniques, 6, 2383-2389, https://doi.org/10.5194/amt-6-2383-2013, 2013.

Knobelspiesse, K., Tan, Q., Bruegge, C., Cairns, B., Chowdhary, J., van Diedenhoven, B., Diner, D., Ferrare, R., van Harten, G., and Jovanovic, V.: Intercomparison of airborne multi-angle polarimeter observations from the Polarimeter Definition Experiment, Applied optics, 58, 650-669, https://doi.org/10.1364/ao.58.000650, 2019.

Knobelspiesse, K. D., Pietras, C., Fargion, G. S., Wang, M., Frouin, R., Miller, M. A., Subramaniam, A., and Balch, W. M.: Maritime aerosol optical thickness measured by handheld sun photometers, Remote Sensing of Environment, 93, 87-106, https://doi.org/10.1016/j.rse.2004.06.018, 2004.

Livingston, J. M., Russell, P. B., Reid, J. S., Redemann, J., Schmid, B., Allen, D. A., Torres, O., Levy, R. C., Remer, L. A., and Holben, B. N.: Airborne Sun photometer measurements of aerosol optical depth and columnar water vapor during the Puerto Rico Dust Experiment and comparison with land, aircraft, and satellite measurements, Journal of Geophysical Research: Atmospheres, 108, 2003.

Macke, A., Kalisch, J., Zoll, Y., and Bumke, K.: Radiative effects of the cloudy atmosphere from ground and satellite based observations, EPJ Web of Conferences, 2010, 83-94,

MAN: AERONET Maritime Aerosol Network database, available at: https://aeronet.gsfc.nasa.gov/new_web/maritime_aerosol_network.html. Last access: 4 February 2019,

Mattis, I., Ansmann, A., Müller, D., Wandinger, U., and Althausen, D.: Multiyear aerosol observations with dual-wavelength Raman lidar in the framework of EARLINET, Journal of Geophysical Research: Atmospheres, 109, https://doi.org/10.1029/2004jd004600, 2004.

Morys, M., Mims III, F. M., Hagerup, S., Anderson, S. E., Baker, A., Kia, J., and Walkup, T.: Design, calibration, and performance of MICROTOPS II handheld ozone monitor and Sun photometer, Journal of Geophysical Research: Atmospheres, 106, 14573-14582, https://doi.org/10.1029/2001jd900103, 2001.

Müller, D., Ansmann, A., Mattis, I., Tesche, M., Wandinger, U., Althausen, D., and Pisani, G.: Aerosol-type-dependent lidar ratios observed with Raman lidar, Journal of Geophysical Research: Atmospheres, 112, https://doi.org/10.1029/2006jd008292, 2007.

Rittmeister, F., Ansmann, A., Engelmann, R., Skupin, A., Baars, H., Kanitz, T., and Kinne, S.: Profiling of Saharan dust from the Caribbean to western Africa-Part 1: Layering structures and optical properties from shipborne polarization/Raman lidar observations, Atmospheric Chemistry and Physics, 17, 12963-12983, https://doi.org/10.5194/acp-17-12963-2017, 2017.

Shin, S. K., Tesche, M., Kim, K., Kezoudi, M., Tatarov, B., Muller, D., and Noh, Y.: On the spectral depolarisation and lidar ratio of mineral dust provided in the AERONET version 3 inversion product, Atmospheric Chemistry and Physics, 18, 12735-12746, https://doi.org/10.5194/acp-18-12735-2018, 2018.

Smirnov, A., Holben, B. N., Kaufman, Y. J., Dubovik, O., Eck, T. F., Slutsker, I., Pietras, C., and Halthore, R. N.: Optical properties of atmospheric aerosol in maritime environments, Journal of the Atmospheric Sciences, 59, 501-523, 2002.

Smirnov, A., Holben, B. N., Slutsker, I., Giles, D. M., McClain, C. R., Eck, T. F., Sakerin, S. M., Macke, A., Croot, P., Zibordi, G., Quinn, P. K., Sciare, J., Kinne, S., Harvey, M., Smyth, T. J., Piketh, S., Zielinski, T., Proshutinsky, A., Goes, J. I., Nelson, N. B., Larouche, P., Radionov, V. F., Goloub, P., Moorthy, K. K., Matarrese, R., Robertson, E. J., and Jourdin, F.: Maritime Aerosol Network as a component of Aerosol Robotic Network, J Geophys Res-Atmos, 114, https://doi.org/10.1029/2008jd011257, 2009.

Smirnov, A., Holben, B. N., Giles, D. M., Slutsker, I., O'Neill, N. T., Eck, T. F., Macke, A., Croot, P., Courcoux, Y., Sakerin, S. M., Smyth, T. J., Zielinski, T., Zibordi, G., Goes, J. I., Harvey, M. J., Quinn, P. K., Nelson, N. B., Radionov, V. F., Duarte, C. M., Losno, R., Sciare, J., Voss, K. J., Kinne, S., Nalli, N. R., Joseph, E., Moorthy, K. K., Covert, D. S., Gulev, S. K., Milinevsky, G., Larouche, P., Belanger, S., Horne, E., Chin, M., Remer, L. A., Kahn, R. A., Reid, J. S., Schulz, M., Heald, C. L., Zhang, J., Lapina, K., Kleidman, R. G., Griesfeller, J., Gaitley, B. J., Tan, Q., and Diehl, T. L.: Maritime aerosol network as a component of AERONET - first results and comparison with global aerosol models and satellite retrievals, Atmospheric Measurement Techniques, 4, 583-597, https://doi.org/10.5194/amt-4-583-2011, 2011.

Stocker, T.: Climate change 2013: the physical science basis: Working Group I contribution to the Fifth assessment report of the Intergovernmental Panel on Climate Change, Cambridge University Press, 2014.

Tesche, M., Ansmann, A., Muller, D., Althausen, D., Mattis, I., Heese, B., Freudenthaler, V., Wiegner, M., Esselborn, M., Pisani, G., and Knippertz, P.: Vertical profiling of Saharan dust with Raman lidars and airborne HSRL in southern Morocco during SAMUM, Tellus Series B-Chemical and Physical Meteorology, 61, 144-164, https://doi.org/10.1111/j.1600-0889.2008.00390.x, 2009.

Toledano, C., Cachorro, V., Berjon, A., De Frutos, A., Sorribas, M., De la Morena, B., and Goloub, P.: Aerosol optical depth and Ångström exponent climatology at El Arenosillo AERONET site (Huelva, Spain), Quarterly Journal of the Royal Meteorological Society: A journal of the atmospheric sciences, applied meteorology and physical oceanography, 133, 795-807, https://doi.org/10.1002/qj.54, 2007.

Willmott, C. J.: Some comments on the evaluation of model performance, Bulletin of the American Meteorological Society, 63, 1309-1313, https://doi.org/10.1175/1520-0477(1982)063%3C1309:scoteo%3E2.0.co;2, 1982.

WMO, W.: GAW Experts Workshop on a Global Surface Based Network for Long Term Observations of Column Aerosol Optical Properties, edited by U. Baltensperger, L. Barrie, C. Wehrli, GAW Report,

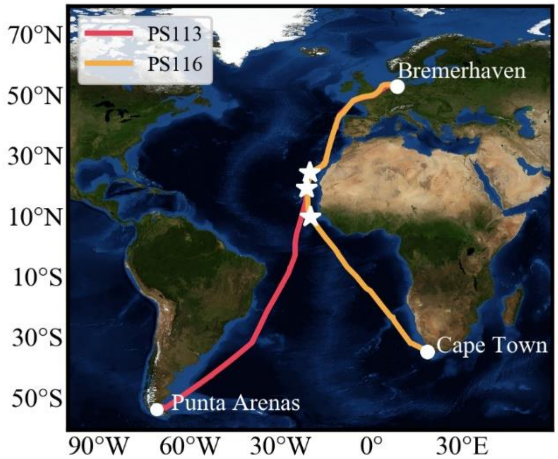

Figure 1. Ship tracks for RV *Polarstern* cruises. PS113 started from Punta Arenas, Chile on 7 May 2018 and arrived at Bremerhaven, Germany on 11 June 2018. PS116 started from Bremerhaven, Germany on 11 December 2018 and arrived at Cape Town, South Africa on 11 December 2018. White stars mark the location of the case studies presented in Sect. 3.

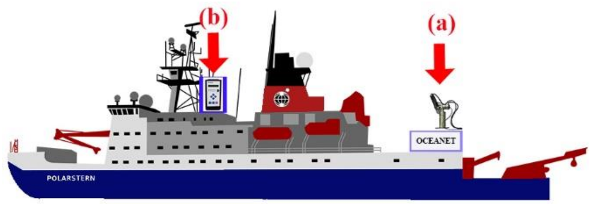

Figure 2 Photometer and lidar observations aboard RV *Polarstern*. MICROTOPS II observations were performed at site (b). Lidar and shipborne CE318-T observations were conducted at site (a).

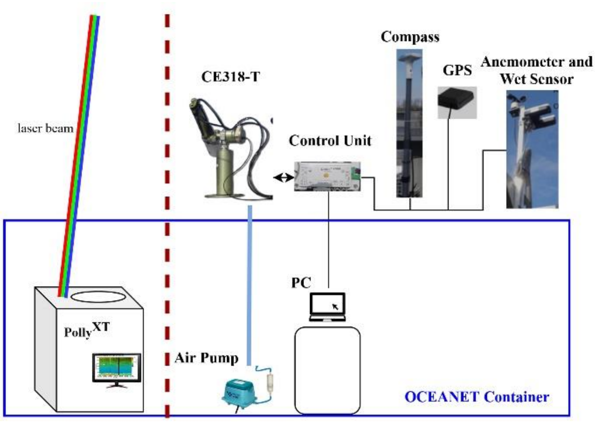

Figure 3. Sketch of the Polly^{XT} lidar (left of the dashed line) and the shipborne CE318-T (right of the dashed line).

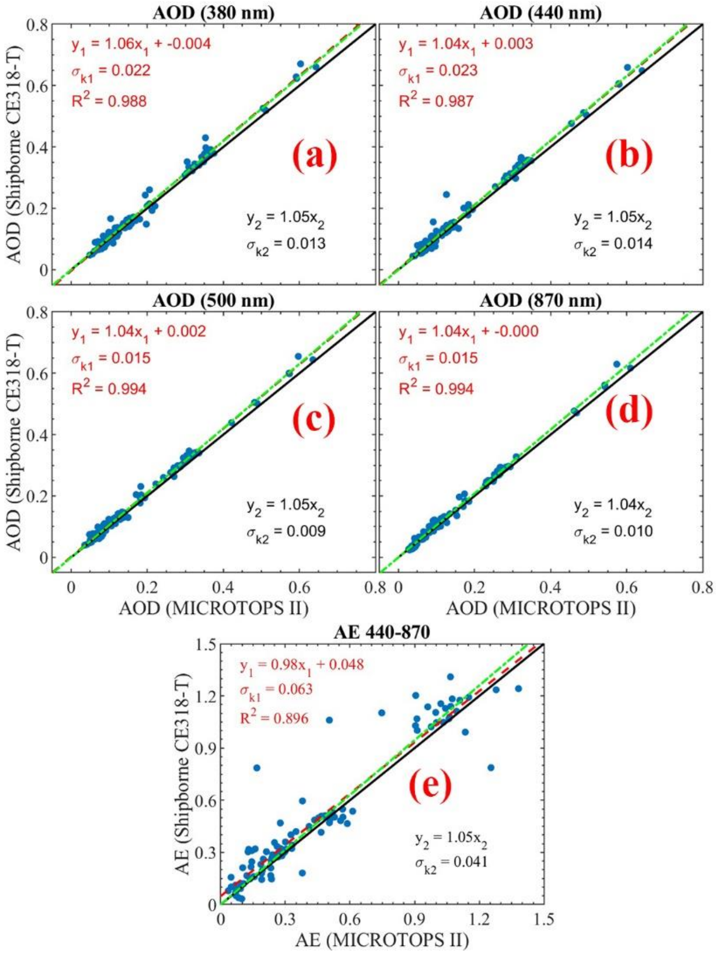

Figure 4. Linear regression of AOD (a, b, c, d) and Ångström exponent (e) from the shipborne CE318-T and MICROTOPS II observations. The data points are the mean values within a sliding window of 20 min. 115 data pairs are used in this regression. The red dashed line is the regression result with free intercept relationship and the green dot-dashed line represents the regression relationship with forced intercept through 0.

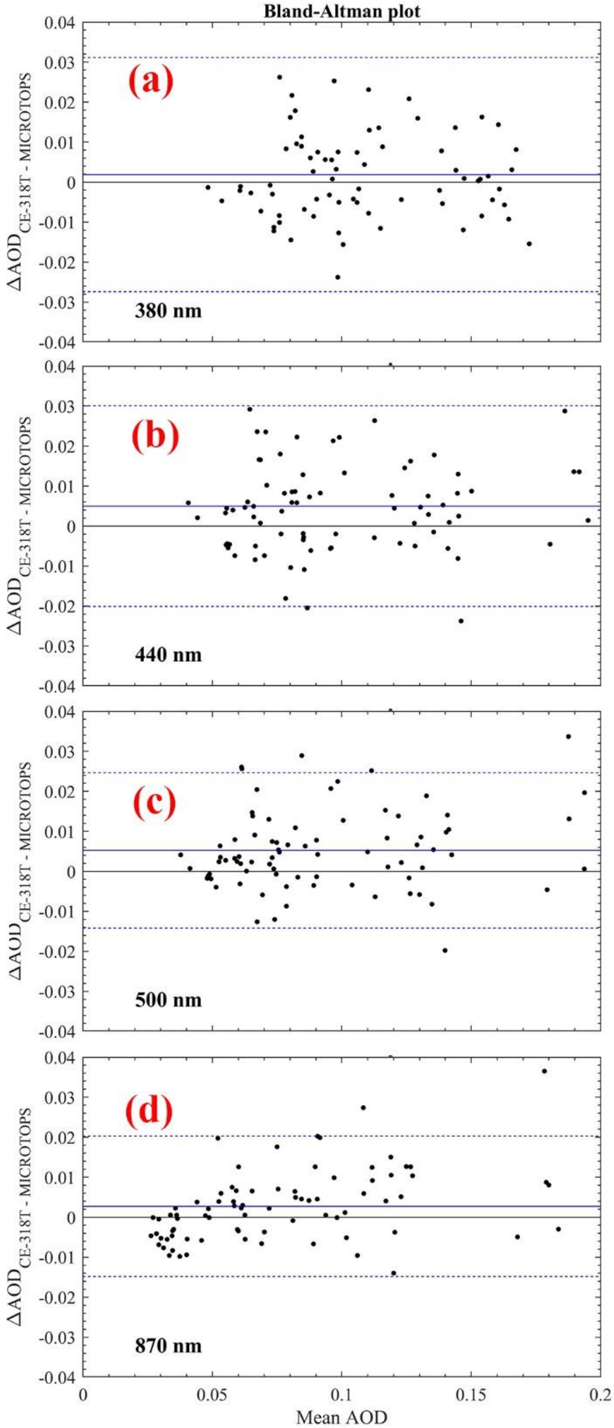

Figure 5. Bland-Altman plots for AOD differences with mean AOD (($AOD_{CE\text{-}318T}$+$AOD_{MICROTOPS}$)/2) at 380 (a), 440 (b), 500 (c) and 870 nm (d). Solid line (black) represents the 0 line. Solid line (blue) represents the mean AOD differences and dotted lines (blue) represent the mean AOD plus/minus the root-mean-squared AOD differences.

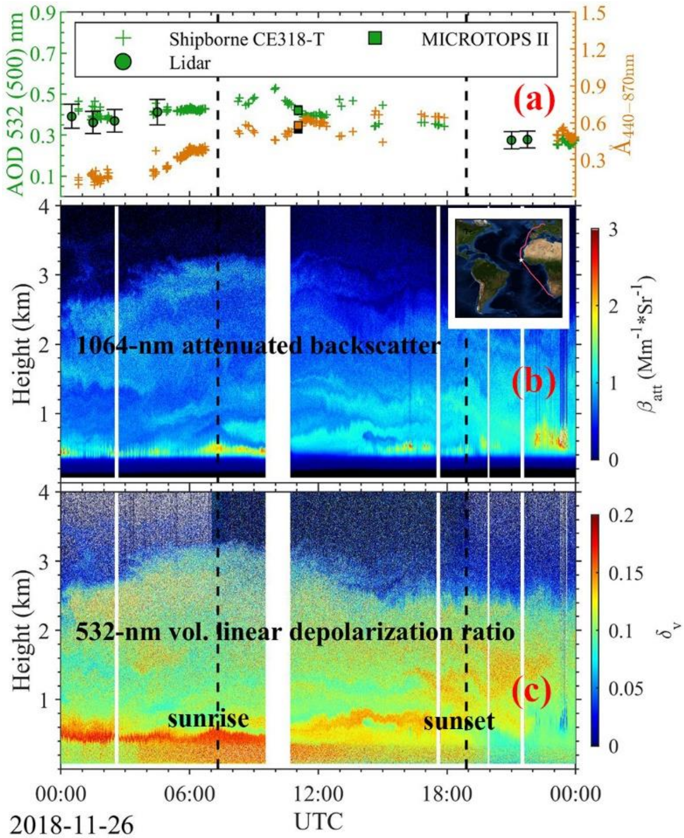

Figure 6. Shipborne aerosol observation with CE318-T, MICROTOPS II and Polly^{XT} lidar at conditions with a mixture of dust and smoke on 26 November 2018. (a) Comparison of 532 nm AOD from shipborne CE318-T and Polly^{XT} lidar observations and 500 nm AOD from MICROTOPS II measurements and Ångström exponent at 440-870 nm obtained from shipborne CE318-T and MICROTOPS II data, (b) mixed layer extended to about 3.5 km height as observed with lidar in terms of 1064 nm attenuated backscatter, and (c) volume depolarization ratio indicating dust-contaminated MBL. The narrow white strips are the lidar depolarization calibration periods and the thick white strip at 10:00 UTC is the routine turn-off time to avoid solar damage at noon.

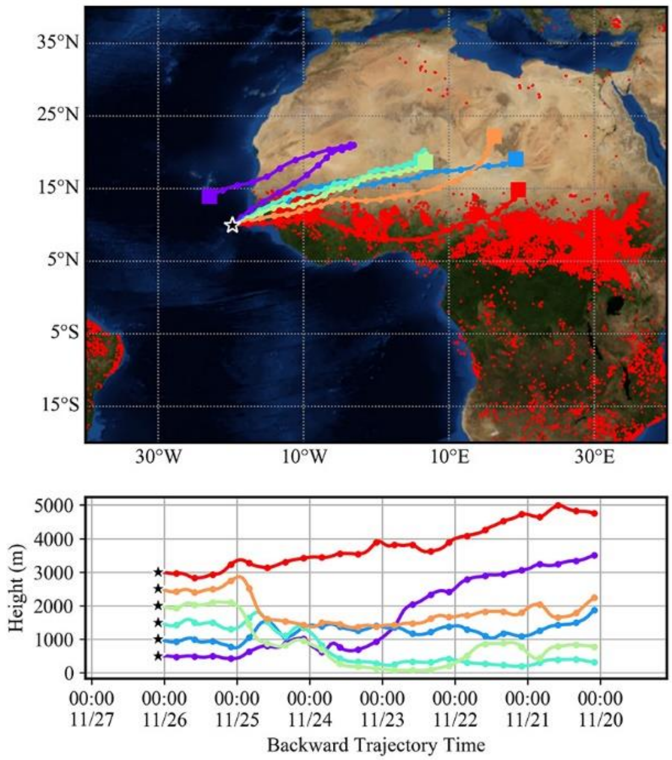

Figure 7. NOAA HYSPLIT backward trajectories arriving at RV *Polarstern* (black star with white border, 10.04 °N, 19.82 °W) on 26 November 2018, 02:00 UTC. Red dots are the fire spots detected by MODIS aboard the Terra and Aqua satellites over the period from 20 November to 26 November 2018 (last access: 4 February 2019).

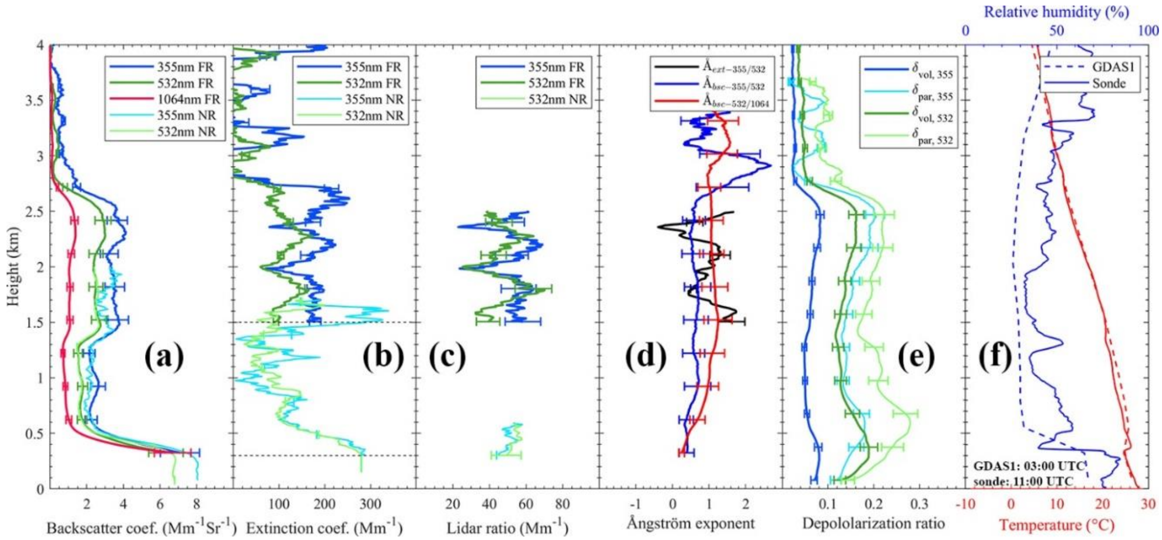

Figure 8. Raman lidar observation on 26 November 2018, 02:00-03:00 UTC. (a) Particle backscatter coefficients, (b) particle extinction coefficients (Raman lidar method), (c) lidar ratio, (d) Ångström exponents computed from different wavelengths pair in (a) and (b), (e) volume (δ_{vol}) and particle (δ_{par}) depolarization ratios, and (f) relative humidity (blue) and temperature (red) from radiosonde observations and GDAS1 dataset.

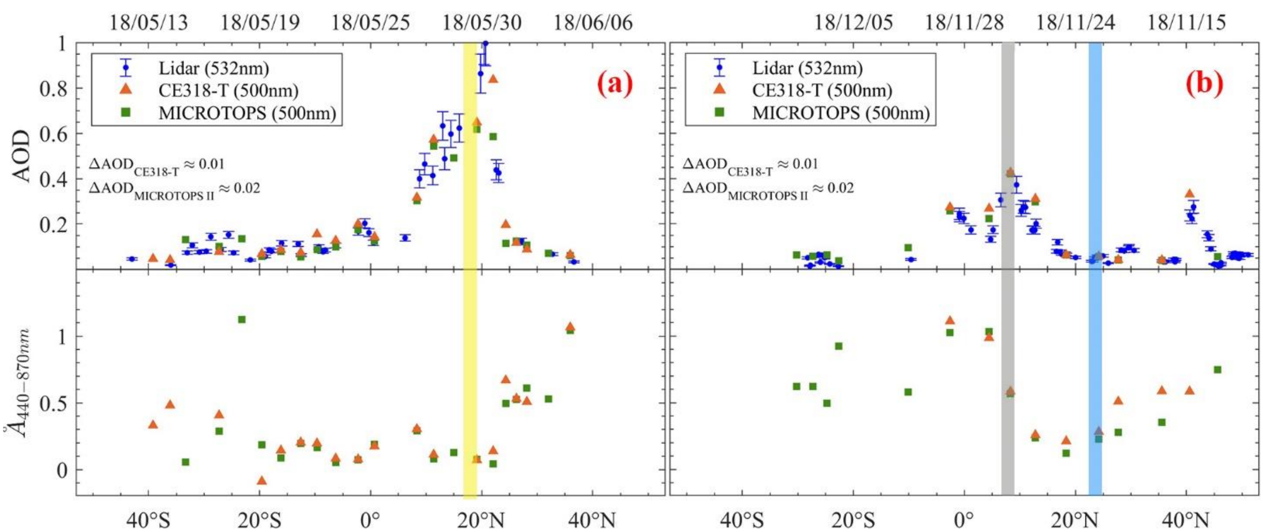

Figure 9. (a) Latitudinal distribution of daily mean AOD measured with Polly^{XT} lidar, MICROTOPS II and shipborne CE318-T. Panel (a) and (b) show the results from PS113 and PS116, respectively. The three colored vertical strips indicate the cases used in Sect. 3.1.2 and Sect. 3.2 (yellow: Saharan dust in Fig. 13, grey: diurnal measurements in Fig. 6, blue: pure marine condition in Fig. 10). Uncertainty in shipborne CE318-T and MICROTOPS II observations are referred to the analysis of Smirnov et al. (2009) and Smirnov et al. (2011).

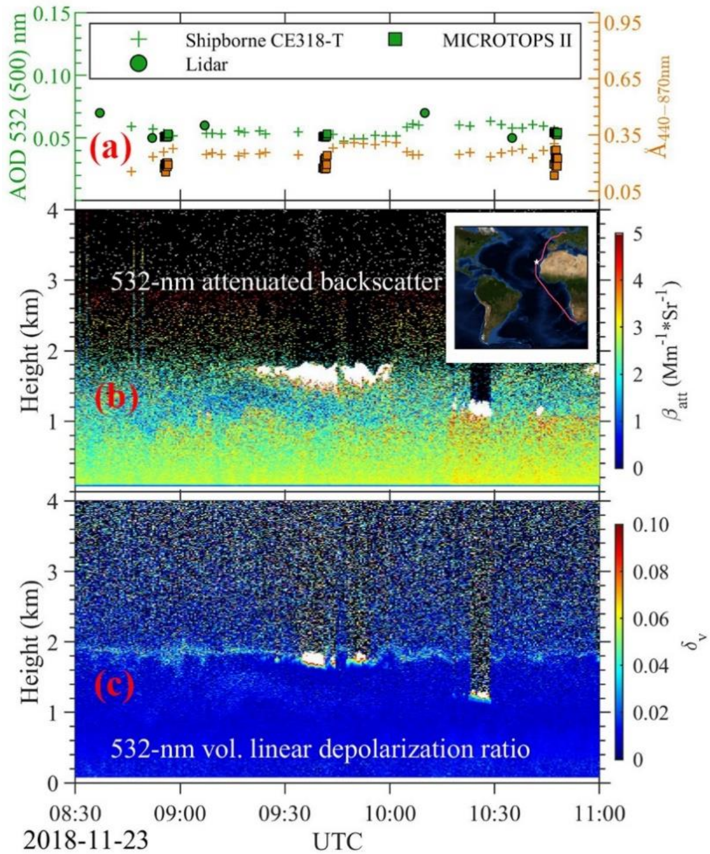

Figure 10. Shipborne aerosol observation with the shipborne CE318-T, MICROTOPS II and Polly^{XT} lidar at pure marine conditions on 23 November 2018. (a) Comparison of 532 nm AOD measured with shipborne CE318-T and Polly^{XT} lidar and 500 nm AOD from MICROTOPS II and Ångström exponent at 440-870 nm from shipborne CE318-T and MICROTOPS II, (b) marine aerosol layer reaching to about 2 km height, partly topped with cumulus clouds (white area), observed with lidar in terms of 532 nm attenuated backscatter, and (c) volume depolarization ratio indicating pure marine condition (very low depolarization ratio caused by the spherical droplets as sea salt particle was deliquescent at RH > 70 %) with dried cubic-like sea salt particles at the top (slightly enhanced depolarization ratio) at RH < 45 %.

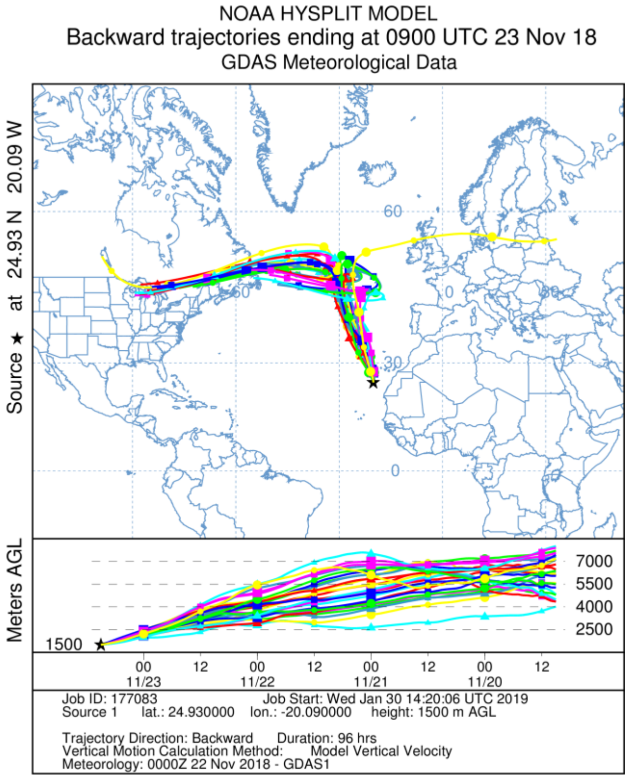

Figure 11. Six-day HYSPLIT backward trajectory ensemble arriving at 1500 m height above RV *Polarstern* (black star, 18.41 °S, 32.93 °W) on 23 November 2018, 22:00 UTC.

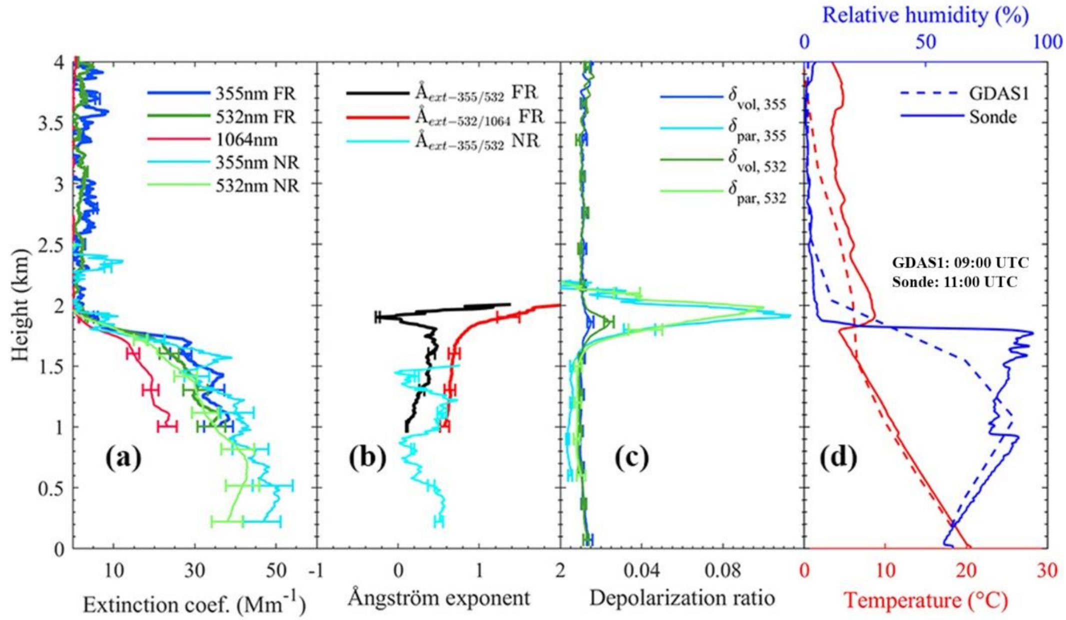

Figure 12 Height profiles of (a) particle extinction coefficients at 355 nm (blue, FR from far-range signal, NR from near-range signal), 532 nm (green), and 1064 nm (red), (b) Ångström exponents computed from different wavelengths pair in (a), (c) volume (δ_{vol}) and particle (δ_{par}) depolarization ratios, and (d) relative humidity (blue) and temperature (red). The lidar observations were taken on 23 November 2018, 08:30 – 09:14 UTC. The radiosonde was launched at 11:00 UTC. GDAS1 data for 09:00 UTC are shown for comparison.

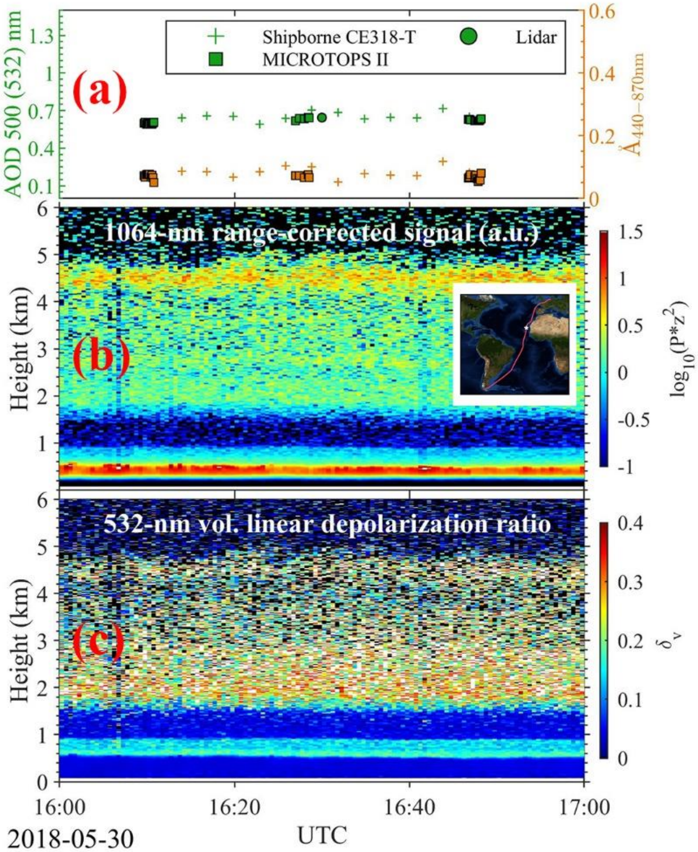

Figure 13. Shipborne aerosol observation with the shipborne CE318-T, MICROTOPS II and Polly^{XT} lidar with strong dust loading on 30 May 2018. (a) Comparison of 500 nm AOD and Ångström exponent at 440-870 nm with shipborne CE318-T and MICROTOPS II, (b) the dust layer extending from 1.5 to 5 km and MBL reaching to 0.6 km, as indicated characterized by the strong range-corrected signal at 1064 nm (red), and (c) volume depolarization ratios indicating the marine layer (low values, blue) and the Saharan dust layer (high values, green and yellow).

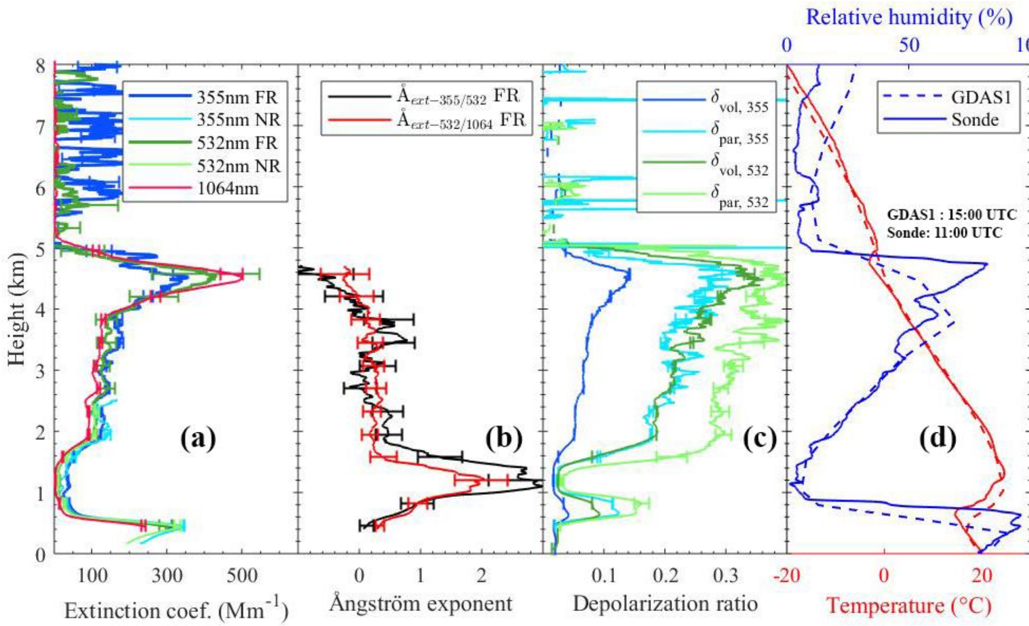

Figure 14. Height profiles of (a) particle extinction coefficients at 355 nm (blue, FR from far-range signal, NR from near-range signal), 532 nm (green), and 1064 nm (red), (b) Ångström exponents computed from different wavelengths pair in (a), (c) volume (δ_{vol}) and particle (δ_{par}) depolarization ratios, and (d) relative humidity (blue) and temperature (red). The lidar observations were taken on 30 May 2018, 16:00 – 16:59 UTC. The radiosonde was launched at 11:00 UTC. GDAS1 data is for 15:00 UTC.

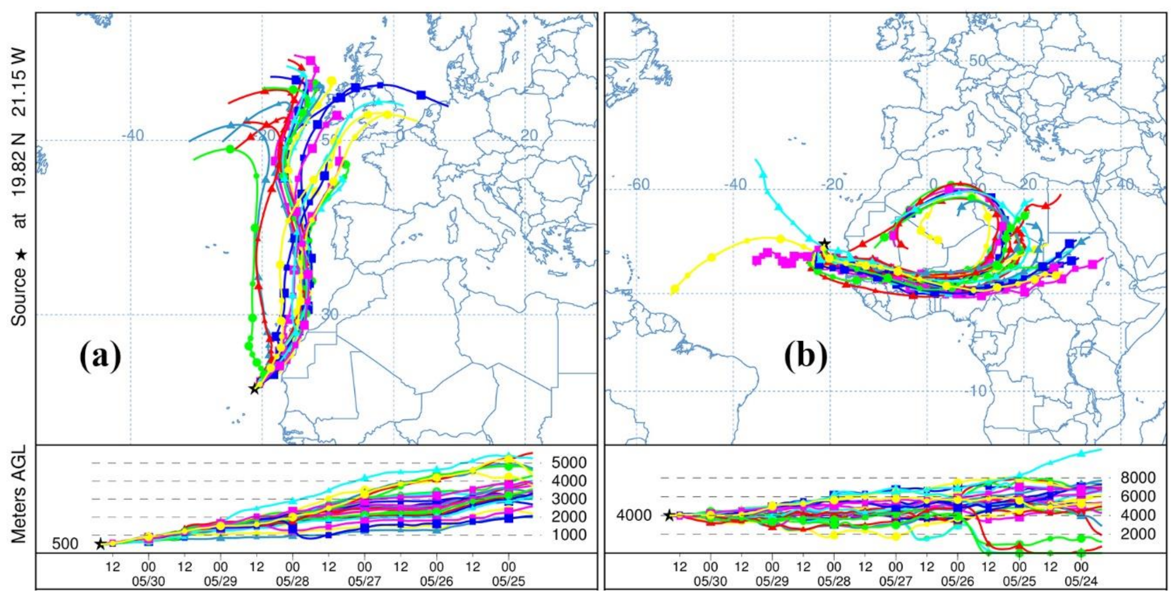

Figure 15. Six-day HYSPLIT backward trajectory ensemble arriving at 500 m (a) and 4,000 m (b) height above RV *Polarstern* (black star) on 30 May 2018, 16:00 UTC.